A&A 449, 1101–1116 (2006)
DOI: 10.1051/0004-6361:20054053

Astronomy & Astrophysics

Water ice growth around evolved stars

II. Modeling infrared spectra

C. Dijkstra[1,2], C. Dominik[1], J. Bouwman[3], and A. de Koter[1]

[1] Astronomical Institute, "Anton Pannekoek", University of Amsterdam, Kruislaan 403, 1098 SJ Amsterdam, The Netherlands
[2] Department of Physics and Astronomy, University of Missouri Columbia, 300 Physics Building UMC, Columbia MO 65211, USA
e-mail: dijkstrac@missouri.edu
[3] Max-Planck-Institut für Astronomie, Königstuhl 17, 69117 Heidelberg, Germany

Received 16 August 2005 / Accepted 19 December 2005

ABSTRACT

We present combined radiative transfer and H_2O ice formation calculations for the dusty envelopes of oxygen-rich evolved stars. We study the effects of various (circum-)stellar parameters on the spectral energy distribution of these stars, their infrared spectral water ice features at 3 μm and in the 30−100 μm region, and the properties of (water ice on) the grains in their envelopes. We also study the ice formation process as a function of stellar evolution for a star with an initial mass of 5 $M_\odot$, which is followed during the AGB, post-AGB and planetary nebula (PN) phase. We find that its water ice features probe its evolution. Both crystalline and amorphous water ice form in our models. The 43 and 62 μm crystalline water ice features are most prominent during the post-AGB phase, and only modestly or not present during the AGB and PN phase, in agreement with observations. The strength of the 3, 43 and 62 μm water ice features decreases with decreasing initial mass of the star. The total amount of ice predicted (a few percent of the total dust mass) also agrees with observations, but the crystalline ice mass fraction is consistently about two orders of magnitude lower. This is mainly due to efficient amorphization by interstellar UV photons, and leads to weaker 43 and 62 μm crystalline water ice features than observed. The intensity of the interstellar UV radiation field strongly influences the strength of these features. We discuss several means to increase the crystalline water ice mass, and hence their strength. The strength of the features increases dramatically when the mass-loss rate over luminosity ratio of the star, $\dot{M}/L$, is large in the AGB phase. In case of the post-AGB star HD 161796 we demonstrate that this indeed leads to the correct crystalline ice mass fraction and feature strengths. Also, the formation of clumps in the AGB wind provides high densities to stimulate the formation of (crystalline) ice. For stars with high initial masses, it additionally provides sufficient shielding from interstellar UV radiation to keep ice crystalline during the post-AGB and PN phase. Axisymmetric mass loss on the AGB provides favorable conditions for the formation and preservation of water ice, and crystalline water ice in particular, as well. In contrast we find that post-AGB crystallization of AGB produced amorphous ice is unimportant for increasing the crystalline water ice mass around 5 $M_\odot$ stars.

Key words. circumstellar matter – infrared: stars – stars: abundances – stars: AGB and post-AGB – stars: infrared spectra – stars: mass-loss

1. Introduction

Asymptotic Giant Branch (AGB) stars are the highly evolved descendants of low and intermediate mass main sequence (MS) stars ($1 \leq M < 8\ M_\odot$), which for a period of some 10^6 yr lose mass at a high rate (10^{-7} to $10^{-4}\ M_\odot$/yr). The outflowing matter creates a dusty molecular circumstellar envelope which may completely obscure the central star. As the dust is driven outwards by radiation pressure of the central star, it drags the molecules in the envelope along with it. Given the right conditions, some molecular species may condense onto the grains as ice farther out in the outflow. After the AGB phase the star starts to shrink in radius at constant luminosity, getting hotter over time. The star is now said to be in the post-AGB phase. The circumstellar envelope, which is expanding away from the star, initially still obscures the central star, but becomes optically thin at optical wavelengths after ∼100−1000 yr. Depending on the rate at which the central star evolves (this is now controlled by both nuclear burning and mass loss), the star may start to photo-ionize the material that was ejected during the AGB phase when $T_{\rm eff} \geq 30\,000$ K, creating a planetary nebula (PN). In this case the phase between the end of the AGB and the birth of the PN is called the proto-planetary nebula (proto-PN) phase. Finally, the star decreases rapidly in luminosity, and eventually becomes a cooling white dwarf (WD). The remains of the circumstellar envelope disperse into the Interstellar Medium (ISM).

In this paper we study the formation and spectral appearance of water (H_2O) ice in the circumstellar envelopes

of evolved stars[1]. Water ice is an important solid state component, which provides information about the physical conditions in these envelopes (see e.g. Jura & Morris 1985; Meyer et al. 1998; Dijkstra et al. 2003a, hereafter called Paper I). It can be detected by its infrared spectral features, and has been observed in the environments of several AGB stars, including OH 26.5+0.6, OH 127.8+0.0, and OH 231.8+4.2 (see Omont et al. 1990, and references therein), and post-AGB stars like M 1-92 (Eiroa & Hodapp 1989) and HD 161796 (Hoogzaad et al. 2002). Water ice has also been suggested to be present in PNe like NGC 6302 (see e.g. Molster et al. 2001). An understanding of the water ice condensation process is important for the appearance and subsequent interpretation of both the solid-state and gas-phase spectral features associated with water (and derived species such as OH) in circumstellar envelopes. These features provide important information on the mass loss history of, and the physical conditions within, the envelope. Finally, ice mantles may be chemically important, e.g. for the formation of hydrous silicates.

In Paper I we presented a detailed model for the description of the growth of water ice on silicate grains in the circumstellar envelopes of oxygen-rich AGB stars and Red Supergiants. It was shown that ice formation becomes more efficient as the mass-loss rate, $\dot{M}$, of the central star increases, and that small dust grains will dominate the ice formation process if they are present in sufficiently large (relative) numbers. The ice formation process can be characterized in terms of the drift velocity, $v_{\rm drift}$, the relative velocity of the dust with respect to the gas. For any given particle size[2], at $v_{\rm drift} \geq 3$ km s^{-1} the ice formation is heavily suppressed by sputtering, i.e. the mechanical removal of ice lattice particles from the surface of the grain by energetic collisions with gas particles. For subsonic drift velocities ($v_{\rm drift} < 0.6$ km s^{-1}) ice formation is highly efficient. Both crystalline and amorphous ice were found to be forming in circumstellar envelopes, by direct deposition of water vapour on the grains.

In this paper we use the model from paper I to calculate the infrared spectra emitted by AGB stars and Red Supergiants under the influence of ice formation. In order to do so we include three modifications to the model. These are discussed in Sect. 2. The layout of the rest of the paper is as follows. In Sect. 3 we describe the observation of water ice in the spectra of evolved stars. Next, in Sect. 4 we apply the model to stars with a range of stellar and circumstellar parameters, and in Sect. 5 we use the model to study the relation between stellar evolution and ice formation. Given the adopted input parameters, the total amount of ice formed in the models is a few percent, in agreement with observations. However, the crystalline ice mass fraction is consistently about two orders of magnitude lower. In Sect. 6 discusses ways to increase the amount of crystalline ice in the models, where an application of the model to the high galactic latitude star HD 161796 will be shown in Sect. 7. Finally, in Sect. 8 we summarize our findings and list our main conclusions.

[1] We loosely refer to evolved stars as either AGB stars, post-AGB stars, PNe, and/or Red Supergiants, the massive counterparts of AGB stars with MS masses $M > 8\,M_{\odot}$.

[2] Throughout this paper we loosely use the word grain or particle *size*, which refers to the *radius* of the grain or particle.

2. The model

In this section we describe the inclusion of i) a particle size distribution for the silicate grains, ii) the calculation of the infrared spectrum of the circumstellar envelope, and iii) the effects of interstellar UV radiation on ice mantles into the ice formation model.

2.1. Particle size distribution

The number density of dust grain cores (i.e. the original grains without the ice mantles) of different sizes is usually described by the local *particle size distribution* (PSD), $f(a_{\rm c}, r)$, which specifies the number of grains per unit volume in a given core size interval, $[a_{\rm c}, a_{\rm c} + {\rm d}a_{\rm c}]$, at distance r from the star. Here $a_{\rm c}$ represents the core size or initial size of a grain. If the grains were only moving with the gas, it is clear that the relative abundances of grains with different initial sizes would be constant. However, the grains do drift relative to the gas, with speeds dependent on the total grain size (i.e. the size of the entire core mantle grain; see Paper I). Therefore, the relative abundances of grains with different initial sizes becomes dependent on the location in the envelope. In order to describe this accurately, we consider the *particle flux distribution* (PFD), $F(a_{\rm c}, r)$, which is the number of grains in a given core size interval, $[a_{\rm c}, a_{\rm c} + {\rm d}a_{\rm c}]$, that passes through a unit area per unit time at distance r from the star. Outside of the refractory dust formation region, this flux, integrated over a spherical surface around the star, is a preserved quantity, i.e. independent of r.

For a star with a given dust mass-loss rate, $\dot{M}_{\rm dust}$, we must have, at an arbitrary distance $r = r_0$ from the star,

$$\dot{M}_{\rm dust} = 4\pi {r_0}^2 \int_{a_{\rm c,min}}^{a_{\rm c,max}} \frac{4}{3}\pi {a_{\rm c}}^3 \rho_{\rm sil} F(a_{\rm c}, r_0) {\rm d}a_{\rm c} \quad (1)$$

where $a_{\rm c,min}$ and $a_{\rm c,max}$ are the minimum and maximum core radii of the dust grains, i.e. the minimum and maximum radii of the grains before ice formation, and $F(a_{\rm c}, r_0)$ is the particle flux distribution at $r = r_0$. $\rho_{\rm sil}$ is the bulk density of a silicate grain (typically $\sim$3300 kg m^{-3}).

$F(a_{\rm c}, r_0)$ is normalized to the dust mass-loss rate using Eq. (1) and can be any arbitrary distribution. Throughout this paper we will assume that it is a powerlaw of the form

$$F(a_{\rm c}, r_0) = F(a_{\rm c,min}, r_0) \left(\frac{a_{\rm c}}{a_{\rm c,min}} \right)^{\beta} \quad (2)$$

where β is the index of the powerlaw. For $F(a_{\rm c}, r)$ we use

$$F(a_{\rm c}, r) = F(a_{\rm c}, r_0) \left(\frac{r_0}{r} \right)^2 . \quad (3)$$

From the PFD $F(a_{\rm c}, r)$ we derive the PSD,

$$f(a_{\rm c}, r) = \frac{F(a_{\rm c}, r)}{v_{\rm dust}(a, r)} = \frac{F(a_{\rm c}, r_0)}{v_{\rm dust}(a, r)} \left(\frac{r_0}{r} \right)^2 \quad (4)$$

where $v_{\rm dust}(a, r)$ is the velocity of the dust with respect to the star. Note that it depends on a, the radius of the complete grain

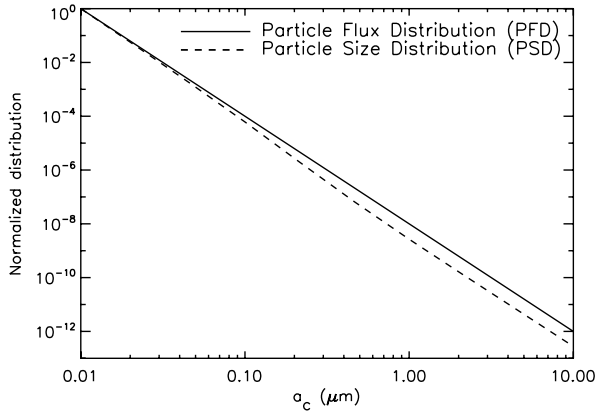

Fig. 1. A comparison of the normalized PFD with the normalized PSD (at $r = r_0$) for model No. 2 in Table 1. For details see Sect. 2.1.

(i.e. core plus ice mantle), and not just a_c (see Paper I for these dependences and how $v_{\rm dust}(a, r)$ is calculated). The number density of dust grains in the core size interval $[a_c, a_c + {\rm d}a_c]$ is now found from the PSD using

$$n_{\rm dust}(a_c, r) = f(a_c, r){\rm d}a_c. \quad (5)$$

For the rate of change in the number density of water molecules in the gas, $n_{\rm H_2O}$, with distance from the star we find

$$\frac{{\rm d}n_{\rm H_2O}}{{\rm d}r} = \sum_{i=1}^{N} -\frac{n_{{\rm dust},i}}{v_{\rm gas}}\frac{{\rm d}N_{{\rm H_2O},i}}{{\rm d}t_i} - \frac{2n_{\rm H_2O}}{r} \quad (6)$$

which is a modified version of Eq. (21) from Paper I. Here $v_{\rm gas}$ is the outflow velocity of the gas with respect to the central star. The index i refers to grains of core size $a_{{\rm c},i}$ and N is the total number of different core sizes. ${\rm d}N_{{\rm H_2O},i}$ is the total amount of water molecules collected by a grain of initial size $a_{{\rm c},i}$, in the time interval ${\rm d}t_i$ that this grain needs to move a distance dr away from the star. The second term on the right hand side of Eq. (6) represents the dilution of water vapour into a larger volume with increasing distance from the central star.

Note that the PFD in Eq. (3) is always a powerlaw with a fixed exponent β, whereas the PSD in Eq. (4) may be different from such a powerlaw, since it depends on $v_{\rm dust}(a, r)$, which also depends on the total grain size. This is demonstrated in Fig. 1, where we compare the PFD with the PSD for model No. 2 in Table 1 (see Sect. 4). Here, the PSD is shown at the inner radius of the envelope ($r = r_0$), and both the PFD and the PSD have been normalized at $a_c = 0.01$ μm. The PFD has a slope $\beta = -4$. The PSD clearly deviates from this. The above effect is strongest for low mass loss rates. As the mass loss rate increases drift velocities generally go down (Paper I), and grains of different sizes will eventually all move at $v_{\rm dust}(a, r) \approx v_{\rm gas}$, yielding a slope for the PSD closer to that of the PFD. Finally, we note that, for the model in Fig. 1, $v_{\rm dust}(a, r)$, and hence the shape of the PSD, does not change strongly as a function of r (a few percent at most for any given initial grain size). The PSD shown for $r = r_0$ may therefore be taken as representative for other distances in this model as well.

2.2. Iteration of the model and calculation of the infrared spectrum

The ice formation process on the dust grains depends on the dust temperature, $T_{\rm dust}$. This quantity is not known a priori as it depends on the optical properties of the dust grains. These in turn depend on the exact details of the ice formation process, and therefore on the dust temperature. In the original model we circumvented this feedback problem by assuming that $T_{\rm dust}$ is given by a powerlaw. Now we will calculate $T_{\rm dust}$ self-consistently. For the gas temperature, $T_{\rm gas}$, which was originally set equal to $T_{\rm dust}$, we will still assume that it is described by a powerlaw.

We self-consistently calculate the dust grain temperature throughout the envelope using an iteration process. In this process we use both our ice formation model and the radiative transfer code MODUST (Bouwman 2001; Kemper et al. 2001), which models the (emergent) spectrum of a spherical dust shell around a central star. First, we use MODUST to make an initial guess for the dust temperature (for each given initial grain size) throughout the envelope. In this first step, the dust density structure for each grain size follows from the assumption that the dust moves at the same speed as the gas (i.e. drift velocities are zero). We also assume that the grains have not yet formed any ice, which sets the optical properties of the grains in this first calculation. Second, the ice formation model calculates the optical properties and densities of the dust throughout the envelope taking into account ice formation, given the initial temperature structure of the dust. Third, the resulting new optical properties and dust densities are given to MODUST, which recomputes the dust temperatures. In this step, the grains generally may contain ice on their surfaces, and will have non-zero drift velocities. Next, the new dust temperatures are fed into the ice formation model, and the above process repeats itself until the dust temperatures and densities have converged to a prescribed accuracy (typically a few percent). Finally, using the converged dust temperatures, densities, and optical properties, we do one more MODUST calculation to calculate the emergent spectrum of the circumstellar envelope.

Note that the interstellar radiation field is taken into account as an outer boundary condition for the intensity in the radiative transfer calculations. The adopted field is applicable for the solar neighborhood (Mathis et al. 1983), which allowed for dust grain temperatures as low as ~20 K.

2.3. Crystalline or amorphous ice: optical properties of grains and the interstellar UV radiation field

As discussed in Paper I, both crystalline and amorphous ice can form in circumstellar envelopes. The deposition rate of water molecules on the surface of the grain combined with the dust temperature, and the presence of an external UV radiation field will determine whether the ice becomes crystalline or amorphous. In Paper I, we considered the formation of both crystalline and amorphous ice, but only included crystalline ice on the surface of the grains for the calculation of the optical properties. As discussed in that paper, this does not greatly affect the ice formation process, but it does affect the spectrum of the

grain and of the circumstellar envelope as a whole. We therefore now include both crystalline and amorphous ice in calculating the optical properties.

To calculate the optical properties for a given grain at a given distance from the star, we first calculate the relative amounts of crystalline and amorphous ice that are present in the icemantle. Given the appropriate fractions, we use an effective medium calculation to obtain the optical constants for the ice mantle. Then, based on the value of the size parameter of the grain, $x = 2\pi a/\lambda$, we either apply a coated sphere calculation (using the routine BHCOAT taken from Bohren & Huffman (1983): used when $x < 30$) or an effective medium calculation in combination with a MIE calculation (Bohren & Huffman (1983): used when $x \geq 30$) to determine the optical properties. The optical constants used in our calculations for the silicate core, the crystalline part of the ice mantle, and the amorphous part of the ice mantle were taken from respectively Suh (1999, cold silicate data), Bertie et al. (1969), and a combination of Warren (1984) and Hudgins et al. (1993). The data are shown in Fig. 2.

To determine the fractions of crystalline and amorphous ice that are present in the icemantle, we should not only consider the relative amounts of crystalline and amorphous ice that have been deposited on the grain, but also the amount of crystalline ice that will be converted to amorphous ice by UV radiation. As discussed in Paper I, in the outflow, initially crystalline ice will form. When the dust temperature drops below ~65 K, the molecules are immobilized on the grain, resulting in amorphous ice. This results in a grain composed of a silicate core surrounded by a layer of crystalline ice, which in turn is surrounded by a layer of amorphous ice. When UV radiation is present, the crystalline part of the ice mantle may potentially be converted to amorphous ice. This will depend on i) the depth up to which the UV radiation can penetrate into the circumstellar envelope, ii) the depth up to which the UV radiation can penetrate into the icemantle, and iii) the time it takes for the ice to become amorphous. We will discuss the latter two effects below.

When an electromagnetic wave enters a solid, the energy of the wave, is given by

$$|E|^2 \propto \mathrm{e}^{-2\delta z} = \mathrm{e}^{-2(2\pi k/\lambda)z} = \mathrm{e}^{-4\pi k z/\lambda} \tag{7}$$

where E is the strength of the electric field of the wave, z is the distance from the surface of the solid, k is the imaginary part of the complex refractive index of the solid and λ is the wavelength of the wave. To find a measure for the depth up to which the wave can penetrate the solid, z_0, we set the exponent in Eq. (7) equal to 1, which then yields

$$z_0 = \frac{\lambda}{4\pi k}. \tag{8}$$

A typical UV photon has a wavelength in the range 2000 Å $\leq \lambda \leq$ 3900 Å where $k \approx 10^{-8}$ for water ice. We thus find that z_0 is of the order of 1 meter, i.e. much larger than the size of a typical ice mantle. The inner crystalline part of the ice mantle can therefore not be effectively shielded from UV radiation, and the ice becomes completely amorphous once UV radiation is present, provided $T_{\rm dust} < 70$ K (Lepault et al. 1983; Kouchi & Kuroda 1990). We have incorporated Eq. (8) into the model to help determine the fractions of amorphous and crystalline ice in detail. This facilitates the calculation of the optical properties, as discussed above.

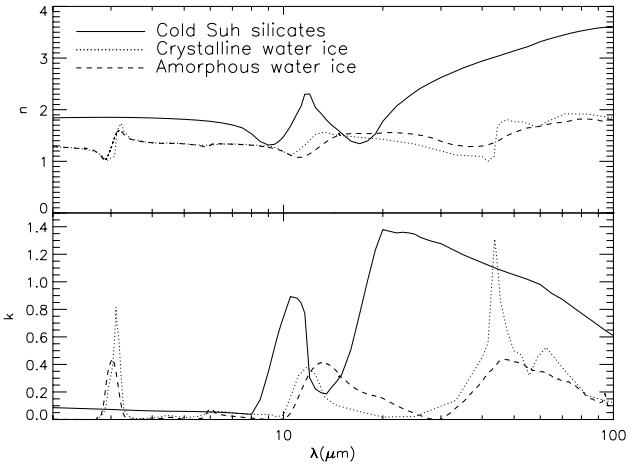

Fig. 2. The optical constants of the materials used in our model calculations. The top panel shows the real part of the complex refractive index, n. The lower panel shows the imaginary part of the complex refractive index, k. For details and the origin of the data see Sect. 2.3.

We use a result of Moore & Hudson (1992) to determine how fast the ice becomes amorphous under the influence of UV radiation. They have shown that, for a given amount of crystalline ice, the unaltered fraction of crystalline ice after a time $t_{\rm rad}$ of irradiation with protons, is given by

$$\Phi(t_{\rm rad}) = \mathrm{e}^{-\kappa D(t_{\rm rad})} = \mathrm{e}^{-\kappa Z_{\rm e} t_{\rm rad}} \tag{9}$$

where $D(t_{\rm rad})$ is the energy dose per molecule (in eV molecule^{-1}) after time $t_{\rm rad}$, κ is the number of molecules destroyed per eV (in molecule eV^{-1}), and $Z_{\rm e}$ is the energy absorption rate per molecule (in eV molecule^{-1} s^{-1}). κ depends on the temperature of the ice, and is larger for lower temperatures (Moore & Hudson 1992). Equation (9) may be applied in case of irradiation with UV photons as well (Hoogzaad 2001), and we thus find for $t_{\rm rad}$

$$t_{\rm rad} = -\frac{\ln(\Phi(t_{\rm rad}))}{\kappa Z_{\rm e}}. \tag{10}$$

To find an upper limit for $t_{\rm rad}$ we consider a typical interstellar UV field between 912 Å and 3900 Å. Such a field has a frequency range $\Delta\nu = 2.5 \times 10^{15}$ Hz and an intensity $I_\nu = 6.3 \times 10^{-8}$ eV s^{-1} cm^{-2} Hz^{-1} sr^{-1} (Black 1994). Next we assume that a molecule within the lattice collects the UV photons from a solid angle $\Delta\Omega = 2\pi$ (since the UV photons mainly come from the travel direction of the grains) over an area $\Delta A = \pi {a_{\rm lattice}}^2 = 6.4 \times 10^{-15}$ cm^2, where $a_{\rm lattice} = 4.5$ Å is the lattice constant of water ice (Kouchi et al. 1994). Then $Z_{\rm e}$ is given by $Z_{\rm e} = I_\nu \Delta A \Delta\nu \Delta\Omega = 6.3 \times 10^{-6}$ eV molecule^{-1} s^{-1}. We also assume that $\kappa \approx 6.5 \times 10^{-3}$ molecule eV^{-1}, which is valid at 70 K (Moore & Hudson 1992). At lower temperatures κ will be larger, and $t_{\rm rad}$ thus smaller. As we are interested in an upper limit for $t_{\rm rad}$, we take the value of κ at 70 K. Finally we require that more than 99% of the ice has turned amorphous, i.e. $\Phi(t_{\rm rad}) = 0.01$, and find $t_{\rm rad} \approx 1.1 \times 10^8$ s or $t_{\rm rad} \approx 3.5$ yr.

The time for the ice to become almost fully amorphous is short compared to the travel time of the grains through the envelope (which is typically in the order of thousands of years). We therefore assume that the grains become amorphous instantaneously, and that there is no broad transition region in the envelope where grains with crystalline ice are converted into grains with pure amorphous mantles. If such a region had existed, it would have been important for the spectrum of the circumstellar envelope and should have been included in the models.

Finally, we note that in order to calculate the distance from the central star up to which the UV photons from the interstellar radiation field are able to penetrate the circumstellar envelope, $R_{\rm UV}$, we used the radiative transfer code MODUST (see Sect. 2.2).

2.4. Remaining assumptions

The model still contains several assumptions that we briefly discuss here for completeness. First, we assume that the sticking probability of each water molecule to the surface of the grain, α, is equal to one. As was discussed in Paper I, this assumption is likely to be correct in the ice formation region of the wind, where temperatures are low ($\leq$100 K) and water molecules stick to an ice surface by means of dipole forces. Initially however, the ice will grow on silicate cores, where the sticking depends on van der Waals forces only, and α may be less than 1. Sticking may also become less efficient at high drift velocities, since incident water molecules may not loose sufficient kinetic energy within the interaction time scale to stay on the grain. In Paper I, we did not treat this velocity dependence of α, since ice growth becomes automatically inefficient at high drift velocities because of sputtering. Still it may confine the ice formation process to even larger mass loss rates and lower luminosities, where drift velocities are low. Unfortunately however, no direct measurements of the above velocity dependence seem to be available in the literature.

Second, we assume that the original silicate grains are not destroyed by sputtering. Also, we ignore chemisputtering, i.e. the removal of ice lattice particles by means of chemical reactions with other species, and grain-grain collisions. This process may remove ice from the surface causing (partial) destruction of grains.

Third, the dissociation of H_2O molecules by the interstellar UV field may lead to a decrease of the available water molecules in the envelope. We have ignored this effect. It will only be important for low mass loss rate stars, where (as was shown in Paper I) sputtering prohibits ice formation.

3. Observations

We now briefly focus on the observations of water ice in the spectra of evolved stars to allow for a better comparison of such observations with our model calculations. As two examples Fig. 3 shows the Infrared Space Observatory (ISO; Kessler et al. 1996) spectra of the OH/IR star OH 127.8+0.0 and the post-AGB star M 1-92. The top panel shows the spectral energy distribution (SED) of these stars. Water ice shows several distinct spectral features at infrared wavelengths. Important features are located near 3 μm (O-H stretch band) and 43 and 62 μm (lattice vibration bands; Bertie et al. 1969). Typically, the 3 μm feature is seen in absorption. The 43 and 62 μm features are mainly seen in emission. A case of absorption at 43 μm is reported for the extreme OH/IR star IRAS 16342-3814 (Dijkstra et al. 2003b). Amongst to other properties, the shape of the spectral features is sensitive to the lattice structure of the ice (see Dijkstra et al. (submitted to A&A hereafter DP05) and references therein).

The lower left and right panels of Fig. 3 show the continuum divided spectra of OH 127.8+0.0 and M 1-92 in respectively the 2.4−4 μm and 30−100 μm region (DP05). Also shown are continuum divided laboratory spectra of crystalline and amorphous water ice. In the 2.4−4 μm region the spectrum of crystalline water ice is characterized by a sharp feature near 3.1 μm with two, unequally strong, shoulders located on either sides of it. The feature minimum is located at relatively long wavelengths (i.e. longwards of 3.0 μm). The spectrum of amorphous ice reveals no significant substructure, and the feature minimum is located at a relatively short wavelength (i.e. near 3.0 μm). In the 30−100 μm region (see also Fig. 2) crystalline ice shows two prominent features near 43 μm and 62 μm. In contrast, amorphous ice only has one very broad spectral feature, making it difficult to distinguish from the continuum in observed spectra. As a result, amorphous ice will hardly show any structure in a 30−100 μm continuum divided spectrum, and will generally be hard, if not impossible, to detect between 30 and 100 μm. Amorphous ice is thus best studied at 3.0 μm.

In the 30–100 μm spectral region, post-AGB stars are found to be dominated by crystalline water ice near 43 and 62 μm, while high mass loss rate AGB (OH/IR) stars and planetary nebulae either show a mixture of crystalline water ice and crystalline silicates, or no crystalline water ice at all (DP05). This is illustrated in the lower right panel of Fig. 3. The 30–100 μm spectrum of the post-AGB star M 1-92 is dominated by crystalline water ice, whereas the OH/IR star OH 127.8+0.0 show crystalline water ice in addition to various other spectral features that can be attributed to crystalline silicates (DP05). For AGB stars, the strength of the observed crystalline water ice features (wrt the continuum) is typically in the order of 10−15% at 43 μm and 5−10% at 62 μm. For post-AGB star, this strength may be as large as 60% at 43 μm and 15% at 62 μm. As stated above, amorphous ice is hard or impossible to detect between 30 and 100 μm when present. Finally, we note that observed 3.0 μm features can be reproduced by a mixture of crystalline and amorphous ice (Fig. 3, lower left panel). The strength of observed 3.0 μm absorption features may range from several percents (see e.g. the probable detection in the OH/IR star OH 26.4-1.9; Meyer et al. 1998) to (almost) complete saturation (see e.g. the post-AGB star IRAS 22036+5306; Sahai et al. 2003).

4. Parameter study: results and discussion

In this section we discuss the results of our model. We will often refer to the *default model*, defined to be the model for an AGB star with a mass loss rate of $\dot{M} = 10^{-4}\ M_{\odot}$/yr,

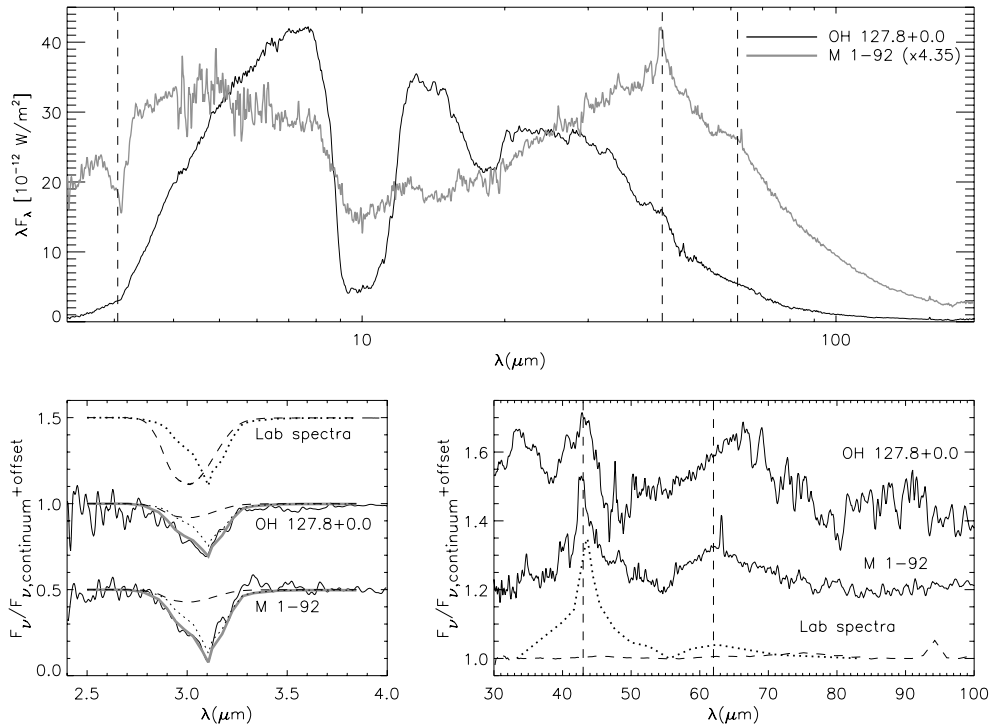

Fig. 3. (*Top panel*) The SED of the OH/IR star OH 127.8+0.0 (black line) and the post-AGB star M 1-92 (grey line). The dashed lines indicate the spectral features of water ice near 3, 43 and 62 μm. For clarity the spectrum of M 1-92 is scaled with a factor 4.35. (*Lower left panel*) The 3 μm continuum divided laboratory spectra of crystalline (dotted line; Bertie et al. 1969) and amorphous (dashed line; Hudgins et al. 1993) water ice fitted to the continuum divided spectra of OH 127.8+0.0 (*middle*) and M 1-92 (*bottom*). The grey lines show the total fits. Offsets are applied to the spectra for clarity. (*Lower right panel*) The 30−100 μm continuum divided spectra of OH 127.8+0.0 (*top*) and M 1-92 (*middle*) compared to the continuum divided laboratory spectra of crystalline (dotted line; Bertie et al. 1969) and amorphous (dashed line; Hudgins et al. 1993) water ice. The dashed lines indicate the 43 and 62 μm crystalline water ice features. The narrow peak at 94 μm in the amorphous ice spectrum is an artifact. Offsets are applied to the spectra for clarity. Results are based on DP05. For details see Sect. 3.

a luminosity $L = 10^4\ L_\odot$, a gas outflow velocity $v_{\rm gas} = 15\ {\rm km\,s^{-1}}$, a PFD powerlaw index $\beta = -4$ (see Eq. (2)), and minimum and maximum initial grain sizes of $a_{\rm c,min} = 0.01\ \mu$m and $a_{\rm c,max} = 10\ \mu$m respectively. The adopted grain size range is motivated by studies on pre-solar grains (e.g. Nittler et al. 1997; Daulton et al. 2003; Clayton & Nittler 2004) and detailed radiative modeling of evolved stars such as IRAS 17150-3224 and HD 161796 (Meixner et al. 2002). The default model corresponds to model 1 in Table 1. We will also often compare our models to *observations*. These observations refer to the general observations listed in Sect. 3, unless a specific reference is explicitly given in the text.

As will be shown in this paper, the crystalline water ice features predicted in our models are very weak. Still, we are interested in studying trends between stellar parameters/evolution and water ice features. Preliminary modelling revealed that by using $\beta = -4$, and thereby favoring small grains which grow ice more efficiently (Paper I), the predicted features are still weak but still sufficiently strong to study trends with stellar evolution. Using $\beta > -4$ (i.e. relatively more larger grains), yielded too weak features for trends to be studied.

Our choise of β affects the total ice mass fraction that will form in the envelope. For $\beta > -4$ more of the dust mass is in larger grains, and less grains are thus available to act as seeds for ice formation. In addition, larger grains form ice less efficiently. Therefore, the total ice mass fraction in the envelope will be less. However, the water ice volume fraction of an individual grain will increase, since more gas-phase water molecules are available per grain. This may affect the optical properties of the grains. The extent of this effect is non-trivial, since it depends on the exact details of the ice formation process. For this reason, we compared the default model and that of HD 161796 (Sect. 7), where $\beta = -4$ in both cases, with similar models where $-4 < \beta \leq -3$. We found that the optical properties of individual grains will only be marginally affected. Finally, we note that our adopted value for β yields a PSD slope larger than the one more commonly adopted for the ISM (-3.5; see Mathis et al. 1977). Still, the ISM size distribution particles may vary from place to place in the Galaxy (see e.g. Kim et al. 1994). Our adopted value of $\beta = -4$ may therefore yet be reasonable.

In Sect. 4.1, we discuss the effects of the mass loss rate, and other (circum-)stellar parameters, on the SED and the infrared spectral features of ice. Section 4.2 addresses the type of ice that forms in the envelope as a function of grain size and distance to the central star.

4.1. Mass loss rate and extreme conditions

We have studied the effect of various stellar and circum-stellar parameters on the SED and the infrared spectral features of ice

Table 1. Details of the ice formation process for the models in Sect. 4.1. Shown are the model number, the depletion Δ, ice over dust mass ratio $M_{\rm ice}/M_{\rm dust}$, and the crystalline over amorphous ice mass ratio $M_{\rm cr}/M_{\rm am}$. The abbreviation *s.g.s* in column 4 refers to a single grain size model where the silicate particles have an initial radius $a_{\rm c} = 0.01\mu$m.

Model No.	$\dot{M}$ ($M_\odot$/yr)	L ($L_\odot$)	$v_{\rm gas}$ (km s^{-1})	β	UV	Δ (%)	$\frac{M_{\rm ice}}{M_{\rm dust}}$ (%)	$\frac{M_{\rm cr}}{M_{\rm am}}$ (%)
1	10^{-4}	10^4	15	-4	on	17.6	2.0	1.0
2	10^{-6}	10^4	15	-4	on	0.7	$\leq$0.1	0.9
3	10^{-5}	10^4	15	-4	on	5.2	0.6	0.9
4	10^{-3}	10^4	15	-4	on	58.5	7.1	0.7
5	10^{-4}	10^4	5	-4	on	68.0	7.8	0.9
6	10^{-4}	5×10^3	15	-4	on	18.0	2.1	1.1
7	10^{-4}	10^4	15	s.g.s	on	44.9	5.5	0.8
8	10^{-4}	10^4	15	-4	off	17.5	2.0	1.0

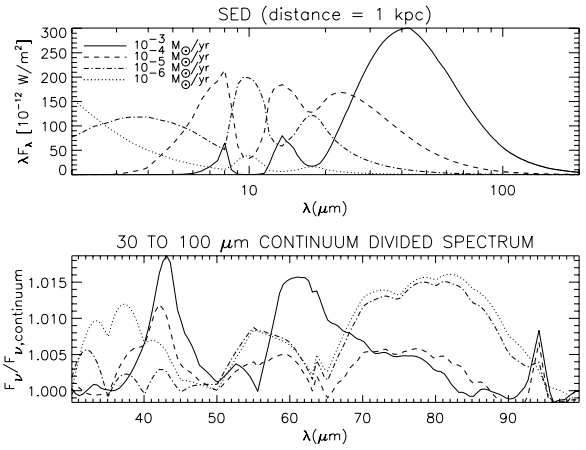

Fig. 4. The SED (*top panel*) and the continuum divided 30–100 μm spectral region (*lower panel*) for stars of different mass loss rates. The mass loss rates are indicated in the upper left corner of the top panel. The line styles in the top and lower panels correspond to the same models. Note that most of the structure seen in the continuum divided spectra is spurious. At these low levels, broad features can easily be the results of uncertainties in the continuum determination, and/or slight slope changes in the optical properties. Only the relatively narrow ice feature at 43 μm can be picked out with confidence. The narrow peak at 94 μm is an artifact in the optical properties of the amorphous ice.

at 3, 43 and 62 μm. The results for the 43 and 62 μm features are shown in Figs. 4 and 5. For all models shown, all parameters, except those explicitly mentioned to be different, are the same as in the default model. Table 1 shows the details on the ice formation process for these models.

Figure 4 shows the SED (top panel), and the continuum divided spectrum from 30 to 100 μm (lower panel), for stars with different mass loss rates (Table 1, models 1 through 4). The SEDs are typical for AGB stars. At low mass loss rates the central star dominates the SED at short wavelengths, and there

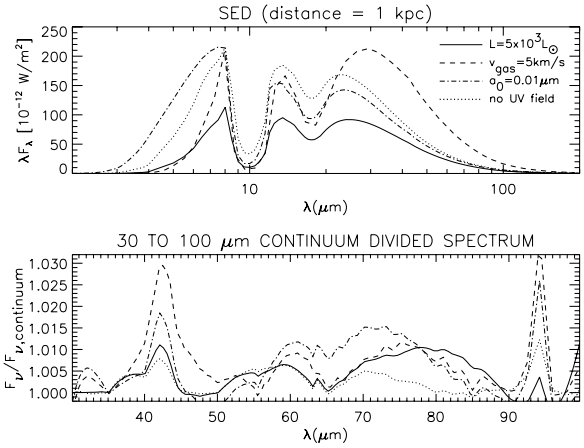

Fig. 5. The SED (*top panel*) and the continuum divided 30–100 μm spectral region (*lower panel*) for stars with different (circum-)stellar parameters. The parameters are indicated in the upper right corner of the top panel. Line styles in the top and lower panels correspond to the same models. See also the caption of Fig. 4.

is an infrared-excess at longer wavelengths showing 10 and 18 μm amorphous silicate emission. At high mass loss rates the central star is no longer visible in the spectrum and only dust emission is seen at long wavelengths. The 10 and 18 μm amorphous silicate features are now in absorption. The 43 and 62 μm water ice features are always weak (see lower panel). They are no stronger than 2% with respect to the continuum, and almost invisible in the SED. Even in cases of extremely high mass loss rates, where we expect ice formation to be highly efficient due to high gas densities and low drift velocities of the grains (Paper I and Sect. 1), the features remain weak. Because of this, the feature shapes in the continuum divided spectra are highly uncertain. In particular this applies to the broad 62 μm feature.

Figure 5 shows the SEDs and continuum divided spectra for AGB stars with a low luminosity, a low gas outflow velocity, envelopes solely composed of small silicate grains of a single size, and envelopes in which an interstellar UV field is absent (Table 1, models 5 through 8). The first three models (models 5, 6 and 7) are extreme cases for which we expect ice formation to be more efficient than in the default model. These models respectively provide low drift velocities, high densities, and more efficient grains for ice formation (see Paper I and Sect. 1). In the last model (model 8) crystalline ice is preserved. The SEDs are dominated by dust emission, and show 10 and 18 μm amorphous silicate absorption features. Once more, the spectral features of water ice near 43 and 62 μm are weak (no stronger than 3% with respect to the continuum), and almost invisible in the SED. Only in model 5 the 43 μm feature is somewhat visible in the SED.

Despite the weakness of the ice features, significant ice formation does occur in all the above models. This is shown in Table 1 where we list Δ, the depletion of water vapour from the gas phase for a volume element located at the outer radius of the envelope. Note that Δ is not the depletion of water vapour from the gas phase for the envelope as a whole. A formal definition of Δ was given in Paper I. In the default model we find $\Delta \approx 18\%$, i.e. at the outer radius of the envelope about 18%

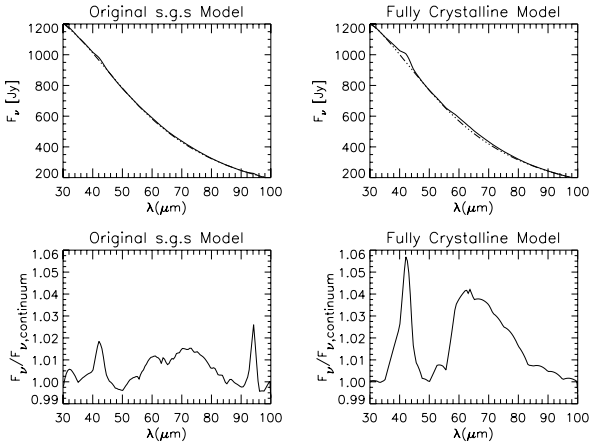

Fig. 6. The effects of ice lattice structure on the 30–100 μm region for model 7 in Table 1. For details see Sect. 4.1.

of the water vapour has been removed from the gasphase. In the cases of extremely high mass loss rates (model 4) and low gas outflow velocities (model 5), Δ becomes as large as 60% to 70%. In both these scenarios the gas density in the envelope is relatively large, and the spectral features at 43 and 62 μm are at their strongest (although still weak). Also in model 7, where we only have small single sized grains of $a_{\rm c} = 0.01$ μm, ice formation is significant ($\Delta \approx 45\%$) and the 43 and 62 μm features are stronger. Models with a high gas density and a large fraction of small dust grains thus provide the most favorable conditions for ice formation to occur, and spectral features to appear. In these models growth rates on the grains are high, and grain drift velocities are small, providing the physical conditions for efficient ice formation.

The weakness of the spectral features is caused by at least two effects. First, the bulk of the ice is amorphous. The crystalline over amorphous ice mass ratio is typically of the order of just $M_{\rm cr}/M_{\rm am} \approx 1\%$ (Table 1). Compared to crystalline ice, which shows distinct 43 and 62 μm features, amorphous ice only has one very broad spectral feature in the 30−100 μm region (Fig. 2), making it difficult to distinguish from the continuum. Second, there is a contrast effect between the spectral features and the (amorphous) silicate continuum. If the silicate continuum emission is strong, the spectral features on top of it will appear to be relatively weak. Finally, a third possible effect is a too low $\dot{M}/L$ ratio in the above models (see Sect. 6.3).

The effect of amorphous ice is seen in Fig. 6, where we show a close up of the 30–100 μm region for the single grain size (s.g.s) model from Table 1 (model 7). The upper left panel shows the original model spectrum (solid line) together with an eyeball estimated continuum (dashed line). The lower left panel shows the resulting continuum divided spectrum (which is the same as the dashed dotted line in Fig. 5). The upper right panel shows a modified s.g.s model spectrum (solid line) and its eyeball estimated continuum (dashed line). In this modified model, we ignore the formation of amorphous ice and the amorphization of crystalline ice. Instead we allow all ice to be crystalline. The corresponding continuum divided spectrum is shown in the lower right panel. Notice the difference in strength of the 43 and 62 μm features. In the modified model the features are 2 to 2.5 times stronger. Figure 6 and Table 1 thus show that substantial amounts of ice (here ∼5% of the total dust-mass) may form, but that the ice will be largely hidden from view in the 30–100 μm spectral region since most of it is amorphous.

We emphasize that the amount of ice formed in the original and modified s.g.s models is almost identical. There are only some minor (<1%) differences in the temperature of the icy dust grains in the ice formation regions (not shown). Also, even though more pronounced, the features in the modified model still appear weak. For all the above models, including the modified s.g.s model, the weakness of the features is due to a contrast effect between these spectral features and the silicate continuum emission. Still, even compared to observations (where the same contrast effect plays a role), the features in the modified model are weak (see e.g. DP05). In most cases, the latter is likely caused by a too low $\dot{M}/L$ ratio (Sect. 6.3).

Finally, none of the models presented in the above parameter study show a 3 μm ice feature, because there is insufficient background continuum emission available near 3 μm due to heavy reddening of the central star. At lower mass loss rates a background continuum may well be available, but here insufficient ice is formed to provide enough column density along the line of sight for ice to be seen in absorption.

4.2. Crystalline and amorphous ice

The transition between crystalline and amorphous ice formation is determined by i) the deposition rate of water molecules on the surface of the grain at a given dust temperature, and ii) the presence of an external UV field, which amorphisizes crystalline ice at dust temperatures below 70 K (Lepault et al. 1983; Kouchi & Kuroda 1990). In paper I we described the first process in terms of the so-called critical flux, $\mathcal{F}_{\rm crit}$. In this case the transition occurs when

$$\mathcal{F}_{\rm gr} = \mathcal{F}_{\rm crit} \tag{11}$$

where $\mathcal{F}_{\rm gr}$ is the growth flux of water molecules, and $\mathcal{F}_{\rm crit}$ is given by

$$\mathcal{F}_{\rm crit} = \frac{D_{\rm s}(0)}{a_{\rm lattice}{}^4} {\rm e}^{-(4590\ {\rm K}/T_{\rm dust})}. \tag{12}$$

Here $T_{\rm dust}$ is the dust temperature, $D_{\rm s}(0) = 17.4$ m^{2}s^{-1} and $a_{\rm lattice}$ is the lattice constant of water ice. When fluxes on the grain surface are low and/or the dust temperature is high ($\mathcal{F}_{\rm gr} < \mathcal{F}_{\rm crit}$), crystalline ice forms. When fluxes on the grain surface are high and/or the dust temperature is low ($\mathcal{F}_{\rm gr} > \mathcal{F}_{\rm crit}$), amorphous ice forms. Both $\mathcal{F}_{\rm gr}$ and $\mathcal{F}_{\rm crit}$ vary with distance from the central star.

In Fig. 7 we show the type of ice that forms in the circumstellar envelope of the default model, as a function of initial grain size and distance from the central star. The figure shows that the inner regions of the envelope form crystalline ice, while the outer regions form amorphous ice. The boundary between the crystalline and amorphous ice formation region is shown as the solid line with stars. The dust grain temperatures at which the transition occurs are indicated and typically between 67 and 71 K. For the small grains (≤1 μm)

Table 2. Details on the ice formation process for a 5 $M_\odot$ star as a function of stellar evolution. The left panel shows the stellar parameters used in our model calculations. The time, t, since the star left the tip of the AGB, was taken (or estimated) from Blöcker (1995a,b). In the right panel we show the details on the ice formation process associated with each model.

Stellar parameters						Ice model results						
phase	t(yr)	$T_{\rm eff}$(K)	$L/L_\odot$	$R/R_\odot$	$\dot{M}$ ($M_\odot$/yr)	Δ (%)	$\frac{M_{\rm ice}}{M_{\rm dust}}$ (%)	$\frac{M_{\rm cr}}{M_{\rm am}}$ (%)	$N_{\rm ice}$ (10^{16} cm^{-2})	$\frac{N_{\rm cr}}{N_{\rm am}}$	$N_{\rm ice}^{\rm obs}$ (10^{16} cm^{-2})	$\frac{N_{\rm cr}^{\rm obs}}{N_{\rm am}^{\rm obs}}$
E-AGB	$-10^{5.6}$	3020	4266	240	8.2×10^{-8}	0.0	0.00		0.00			
TP-AGB	$-10^{3.1}$	3516	23988	407	8.6×10^{-5}	14.3	1.61	0.89	2.76	0.68		
Tip-AGB	0	2500	17458	706	1.6×10^{-4}	18.5	2.09	1.61	8.92	0.85		
post-AGB	101	2537	17498	686	0		2.10	1.61	8.92	0.85	5.94	3.25
post-AGB	303	2611	17498	648	0		2.12	1.61	8.91	0.85	8.45	0.95
post-AGB	505	2686	17498	613	0		2.14	1.53	8.33	0.73	8.00	0.86
post-AGB	1006	2874	17498	535	0		2.16	0.48	5.44	0.13	5.84	0.37
post-AGB	1975	3266	17498	414	0		2.19	0.00	3.08	0.00	4.49	0.00
post-AGB	3995	4462	17498	222	0		2.22	0.00	1.52	0.00	2.37	0.00
post-AGB	5012	7345	17498	82	0		2.22	0.00	1.16	0.00	2.33	0.00
PN	7770	$10^{5.3}$	526	$10^{-1.7}$	0		2.23	0.00	0.73	0.00		

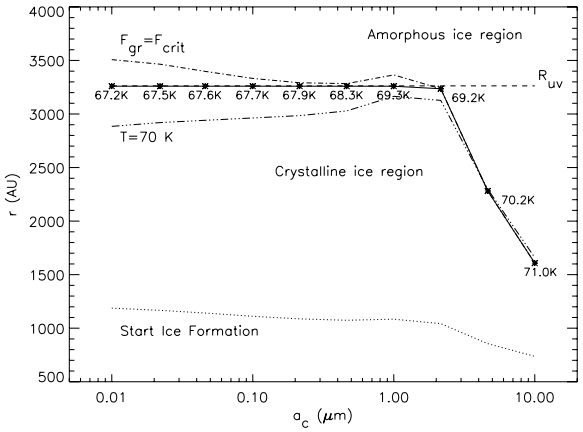

Fig. 7. Crystalline and amorphous water ice formation as a function of initial grain size, $a_{\rm c}$, and distance to the central star, r, for the default model. The *dotted* line shows where ice formation starts. The *dashed triple dotted* line shows where the dust temperature is 70 K. For more details see Sect. 4.2.

the transition coincides with the dashed line, which indicates the distance, $R_{\rm UV}$, up to which UV radiation is able to penetrate the envelope. Outside $r = R_{\rm UV}$, grains are amorphisized by UV radiation if $T_{\rm dust} < 70$ K (Lepault et al. 1983; Kouchi & Kuroda 1990). For the larger grains (>1 μm) the transition occurs at $r < R_{\rm UV}$, and coincides with the dashed dotted line, which indicates where $\mathcal{F}_{\rm gr} = \mathcal{F}_{\rm crit}$. The transition for the large grains is thus initiated by a large flux of water molecules on the surface combined with a low dust temperature, which makes $\mathcal{F}_{\rm gr} > \mathcal{F}_{\rm crit}$. The inner crystalline part of the ice mantle is amorphisized later, when $r \geq R_{\rm UV}$. Note that large grains start forming ice relatively close to the star because of their relatively low temperatures.

We thus find that the physical mechanism for the transition of crystalline to amorphous ice formation will depend on the grain size. Figure 7 shows that as a large grain ($\gtrsim$2 μm) moves through the envelope, it is initially composed of silicates only. As it enters the ice forming region a crystalline ice layer will form. This results in a silicate grain with a crystalline ice mantle. Then the grain enters the amorphous ice formation region, where a silicate grain with an inner crystalline ice mantle and an outer amorphous ice mantle forms. This is caused by the low dust temperature, and relatively high fluxes of water molecules on the grain's surface. Eventually the complete ice mantle becomes amorphous due to UV radiation. In case of a small grain, the ice that initially forms will be crystalline, and is then amorphisized below 70 K by UV radiation. Later, the ice that forms is amorphous upon deposition on the grain surface.

5. Stellar evolution and ice formation

We now study the ice-formation process as a function of stellar evolution. We consider a 5 $M_\odot$ zero age main sequence (ZAMS) star, and follow it from the early AGB phase until the (very late) PN stages. Table 2 and Fig. 8 show the evolution of the star from the AGB onwards. We used a simplified procedure to estimate basic stellar parameters from detailed evolutionary calculations provided by Blöcker (1995a,b). These calculations cover the early AGB to late PN stages, and include a detailed treatment of AGB phase mass loss. More advanced procedures to estimate basic stellar parameters may be applied (Hurley et al. 2000; Izzard et al. 2004). However, our currently adopted procedure is sufficient to study the basic relation between stellar evolution and ice formation.

For a detailed description of the evolution of stars towards and on the AGB we refer to Blöcker (1995b), Habing (1996), Izzard et al. (2004) and Habing & Olofsson (2004, chapter by Lattanzio and Wood). For the post-AGB phase onwards we refer to e.g. Vassiliadis & Wood (1994a,b) and Blöcker (1995a). From here on we will often refer to *tip of the AGB models*, which represent the stars near the very end of the AGB phase, when their mass loss is most extreme.

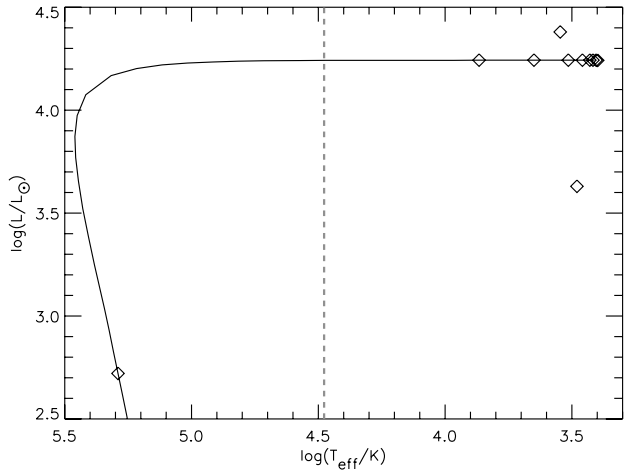

Fig. 8. The evolutionary track of a 5 $M_\odot$ star from the early AGB to the white dwarf phase. The track is based on Blöcker (1995a,b). Diamond symbols indicate points on the evolutionary track where we performed our ice model calculations. The solid line represents the post-AGB track of the star (Blöcker 1995a). The dashed line indicates the point where the effective temperature $T_{\rm eff}$ = 30 000 K, above which the star enters the PN phase.

5.1. Stellar parameters

According to Blöcker (1995b) the mass loss rate of an AGB star, with $M_{\rm ZAMS} > 2\ M_\odot$ and a pulsation period of $P_0 > 100$ days, is given by

$$\dot{M} = 4.83 \times 10^{-9} \left(\frac{M}{M_\odot}\right)^{-2.1} \left(\frac{L}{L_\odot}\right)^{2.7} \dot{M}_{\rm R} \quad [M_\odot/{\rm yr}] \qquad (13)$$

where $\dot{M}$ is the mass loss rate, M is the current stellar mass, and L is the luminosity of the AGB star. $\dot{M}_{\rm R}$ is the Reimers mass loss rate given by

$$\dot{M}_{\rm R} = 4 \times 10^{-13}\, \eta_{\rm R} \frac{(L/L_\odot)(R/R_\odot)}{(M/M_\odot)} \quad [M_\odot/{\rm yr}] \qquad (14)$$

where we use $\eta_{\rm R} = 1$ (see Blöcker 1995b). For a star with a pulsation period of $P_0 \leq 100$ days the Reimers mass loss rate may be used (Blöcker 1995b). If we assume that the star pulsates in its fundamental mode, P_0 is given by

$$\log\left(\frac{P_0}{\rm days}\right) = -1.92 - 0.73 \log\left(\frac{M}{M_\odot}\right) + 1.86 \log\left(\frac{R}{R_\odot}\right) \qquad (15)$$

where R is the stellar radius.

Table 2 lists the stellar parameters used in our calculations. The E-AGB (Early-AGB) model represent an AGB star with a $P_0 = 100$ day period, for which the luminosity, L_0, can be calculated using (Blöcker 1995b)

$$\log\left(\frac{L_0}{L_\odot}\right) = 3.08 + 0.78 \log\left(\frac{M}{M_\odot}\right). \qquad (16)$$

We use this model as our starting point, since the integrated mass loss is small until the star reaches a 100 day pulsation period (Blöcker 1995b), and we thus expect ice formation to be unimportant until this time. The parameters in Table 2 for this model were found using $P_0 = 100$ days and $M = M_{\rm ZAMS}$. R and L (here L_0) were then calculated directly from Eqs. (15) and (16). $\dot{M}$ follows from Eq. (14).

The TP-AGB model represents the star during the Thermal Pulsing AGB phase, a phase in which periods of enhanced mass loss and increased luminosity repeatedly occur. For this model we estimate $T_{\rm eff}$, L, and R from Fig. 5 presented by Blöcker (1995b), after which $\dot{M}$ was found from Eqs. (13) and (14) assuming $M = M_{\rm ZAMS}$ (i.e. we ignore previous mass loss). The TP-AGB parameters are valid for the 10th thermal pulse cycle at phase $\phi = 0.9$ (Blöcker 1995b).

The Tip-AGB (tip of the AGB) model represents the star near the very end of the AGB phase, when the star suffers maximum mass loss. For this model we expect the ice formation process to be most efficient. Here we estimate $\dot{M}$ from Fig. 7 presented by Blöcker (1995b). Since for this point in stellar evolution, $T_{\rm eff}$, L, and R are not provided by Blöcker (1995b), we assume that L is given by the luminosity of the star in the post-AGB phase (see below). For the assumed value of L, we then take representative values for $T_{\rm eff}$ and R using Fluks (1998), who shows the fundamental parameters and other basic properties of M-giant stars as a function of spectral subtype. It can be shown that the circumstellar envelopes in our tip of the AGB models are sufficiently optically thick to reprocess all the stellar radiation in the inner layers of the envelope. The exact shape of the stellar spectrum, which is set by $T_{\rm eff}$, is then irrelevant for the ice-formation process and the spectrum emitted at the outer radius of the envelope.

For the above AGB models, the inner radius of the circumstellar envelope is set by the condition $r_{\rm min} = r(T_{\rm dust} \approx 1000\,{\rm K})$. The total time a star of mass M can lose mass at a rate $\dot{M}$ is $M/\dot{M}$. After this time the outer radius of the circumstellar envelope is $r_{\rm max} = v_{\rm gas} \times (M/\dot{M})$. However, the typical outer radius of old PNe (Weinberger et al. 1983) is observed to be 0.7 pc. We thus set the outer radius of the envelope equal to $r_{\rm max} = \min(v_{\rm gas} \times (M/\dot{M}), 0.7\ {\rm pc})$. Note that we ignore complex structures in the wind (e.g. multiple shells) induced by variable, and increasingly higher, mass loss during the AGB phase.

When the star enters the post-AGB phase, the remnant AGB envelope will move away from the central star. Since the grains do drift relative to the gas (Sect. 2.1), with speeds dependent on the grain size, it is clear that the expansion of the envelope is not characterized by a single expansion velocity. This substantially complicates the description of the geometry of the envelope as soon as it leaves the AGB, and is beyond the scope of this paper to be taken into account. In order to model the post-AGB, PN and WD phases anyhow, we assume that the envelope expansion speed is set by $v_{\rm gas}$. The inner radius will be set by $r_{\rm min} = v_{\rm gas} \times t$, where t is the time since the star left the tip of the AGB (see Table 2), while the outer radius remains the same as on the tip of the AGB. The latter may be justified if the original AGB envelope already extended into the local ISM. Moreover, the outer radii used in our model calculations are sufficiently large such that the dust located at these distances will not contribute to the spectral regions of interest in our study (i.e. wavelengths shorter than 200 μm).

For the post-AGB and PN phase, the grain properties at each distance from the star will be assumed to be the same as those in the original AGB envelope. For these phases we

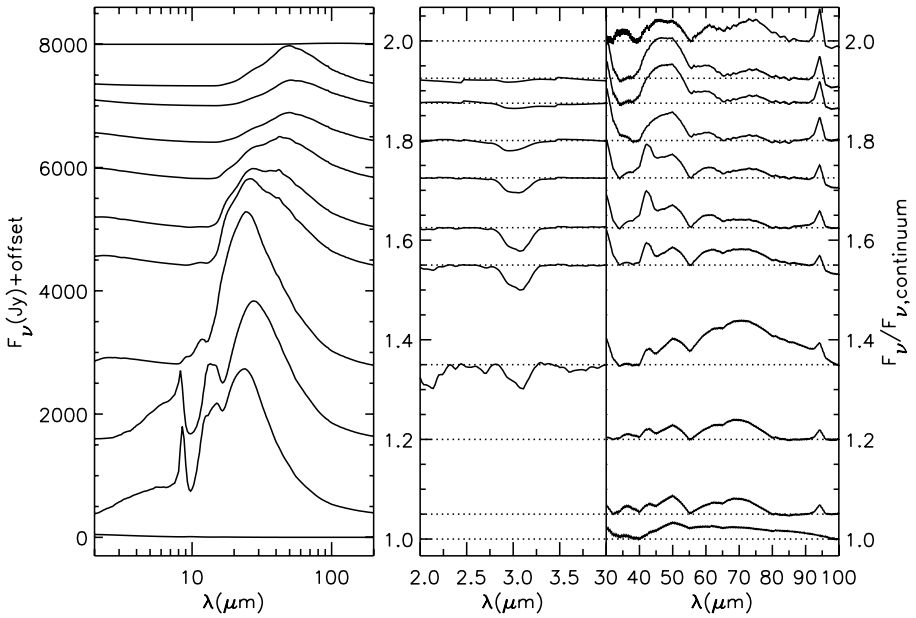

Fig. 9. The infrared (continuum divided) spectrum of a 5 $M_\odot$ star as a function of time for the models listed in Table 2. For details see Sect. 5.2.

will further assume that the mass loss rate of the central star is zero. The 5 $M_\odot$ star will be assumed to follow the H-burning track for a 0.836 $M_\odot$ central star given by Blöcker (1995a). The post-AGB track is shown in Fig. 8. Note that contrary to Blöcker (1995b), who assume a gradual decrease of the mass loss rate between maximum mass loss on the AGB and the post-AGB phase, we will assume an *abrupt* decrease. This is motivated by observations of post-AGB stars such as HD 161796, which imply very high mass loss rates until the onset of the post-AGB phase.

As a final remark, we note that for the spectra in these evolutionary calculations we will use amorphous olivine for the silicate grains, contrary to the Suh-silicates used in Sect. 4. Although the Suh-silicates represent a typical mixture of the materials in the circumstellar envelopes of AGB stars, we found that these silicates may still yield some spurious spectral features that complicate the study of water ice during post-AGB evolution. The model results are expected to be nearly identical in both cases. However, we expect that the amorphous olivines may yield slightly more realistic spectra, in particular in the 10 to 20 μm region. The optical properties for the amorphous olivine were taken from Dorschner et al. (1995). All other dust properties are assumed to be same as for the default model presented in Sect. 4.

5.2. The ice-formation process vs. stellar evolution

In Fig. 9 we show the results of our ice model calculations for the 5 $M_\odot$ star. The spectrum of the star is seen at various evolutionary phases. From left to right the panels show the 2–200 μm spectrum of the star, the continuum divided 2–4 μm spectrum, and the continuum divided 30–100 μm spectrum. Time increases from bottom to top, and each successive spectrum corresponds to a successive time entry in Table 2. The dotted lines in the middle and left panels represent the continuum. In case no clear spectral features were seen in a continuum divided spectrum, it was omitted from the figure. Offsets have been applied to the (continuum divided) spectra for clarity.

5.2.1. The 2–200 μm SED

The left panel of Fig. 9 shows that as the star evolves from the E-AGB to the tip of the AGB (bottom three spectra), the 10 and 18 μm amorphous silicate features go into (self)-absorption. Meanwhile, the overall SED becomes redder. These effects are the result of increasing mass loss during the AGB phase, and have been well studied by previous authors (e.g. Sylvester et al. 1999a, and references therein). After the AGB phase, the circumstellar envelope detaches from the central star and the envelope becomes optically thin. As a result the amorphous silicate absorption features disappear. The peak position of the SED moves to longer wavelengths, caused by the gradual decrease of the temperature in the envelope. The lowering of the temperature is not completely monotonous. In Fig. 9 it can be seen that in the late stages of the post-AGB/PN evolution the envelope may temporarily be reheated. This occurs when the central star starts to emit efficiently at wavelengths shortwards of ∼0.2 μm. At these wavelengths amorphous ice absorbs radiation very effectively, which leads to a temporal reheating of the envelope, and a shift of the peak position of the SED to shorter wavelengths. We return to this effect in Sect. 6.1.

5.2.2. The 3 μm feature

In the middle panel of Fig. 9 we monitor the 3 μm water ice feature as the stars evolve. The feature first appears during the post-AGB phase, some 100 yr after the tip of the AGB. Earlier in the evolution of the star there is already a column of ice present (see Table 2), but then there is insufficient continuum background for the 3 μm feature to be seen. Initially,

the feature shows both crystalline and amorphous ice, characterized by a narrow feature near 3.1 μm, and a broad *shoulder* shortwards of this feature. Later during the post-AGB phase, the feature shifts to shorter wavelengths, and eventually shows amorphous ice only.

The behavior of the 3 μm feature can be explained by the existence of the inner crystalline and outer amorphous ice formation regions discussed in Sect. 4.2 and Paper I. Depending on the relative sizes of these regions, and the densities within each of them, each type of ice may dominate the column density at 3.0 μm. Early in the post-AGB phase, the inner boundary of the envelope moves through the crystalline ice formation region. As long as the inner boundary is inside this region (or closer to the central star), both crystalline and amorphous ice will contribute to the column density at 3.0 μm and will be seen in the spectrum. During later phases, the inner boundary of the envelope will leave the crystalline ice formation region, and enter the amorphous ice formation region. From then on, only amorphous ice contributes to the column density at 3.0 μm, and crystalline ice will no longer be seen in the spectrum. Eventually the complete 3.0 μm feature disappears from the spectrum due to the dilution of the envelope.

In the right panel of Table 2 we list the column density of ice, $N_{\rm ice}$, calculated directly from our models. Also shown is the crystalline over amorphous ice column density ratio, $N_{\rm cr}/N_{\rm am}$. Both $N_{\rm ice}$ and $N_{\rm cr}/N_{\rm am}$ decrease with time in the post-AGB and PN phase, in agreement with our findings above. Table 2 also shows the column density, $N_{\rm ice}^{\rm obs}$, and the crystalline over amorphous ice column density ratio, $N_{\rm cr}^{\rm obs}/N_{\rm am}^{\rm obs}$ as *measured from the predicted spectra*. These measured quantities were found by fitting the 3 μm features in Fig. 9 with spherical ice grains using Mie theory. Most of the measured values are in reasonable agreement with those calculated directly from the model, and show a similar behavior with time. Remaining discrepancies may be attributed to either the weakness of the 3 μm feature at a given time, or uncertainties in the choice of the continuum. Note that the column densities listed in Table 2 are smaller than those typically found for high mass loss rate OH/IR stars and post-AGB stars (see e.g. Meyer et al. 1998; Sylvester et al. 1999b, and DP05), although in agreement with values found by Charnley & Smith (1993) for several OH/IR stars. Whereas we find values of $\sim 10 \times 10^{16}$ cm^{-2} at most, the observed values may be $\sim 50 \times 10^{16}$ cm^{-2} or more. We come back to this point in Sect. 6.3.

5.2.3. The 43 and 62 μm features

In the right panel of Fig. 9 we show the 43 and 62 μm water ice features as the star evolves. As for the models presented in Sect. 4, the features are generally weak, and as a consequence their shape is difficult to determine. In particular the shape of the broad 62 μm band is ill-defined. Still, a clear trend can be observed for the 43 μm feature. Initially, during the AGB phase, water ice is hardly seen in the spectrum, although it does form (see Table 2). As explained in Sect. 4, this is caused by the fact that the bulk of the ice is amorphous and there is a contrast effect between the water ice features and the strong continuum generated by the amorphous silicates in the envelope. In the early post-AGB phase however, some 500 yr after the tip of the AGB (right panel Fig. 9, 6th spectrum from the top), the strength of the water ice features increases and crystalline water ice becomes apparent in the spectrum near 43 μm. The increasing strength of the features is a result of the expanding circumstellar envelope. This removes the strong continuum emission generated by warm dust particles close to the central star, from the spectrum. As a result the visibility of the spectral features is enhanced. As the star continues its post-AGB evolution, the crystalline water ice disappears from the spectrum again. This is due to ongoing amorphization of the ice by UV radiation from the interstellar medium. The general trend described above, is in agreement with DP05, who find observationally (see Sect. 3) that in the 30–100 μm spectral region post-AGB stars have strong crystalline water ice features, while high mass loss rate AGB stars and PNe only show modest crystalline water ice features, or none at all.

In Table 2 we list the depletion of water vapour from the gasphase at the outer radius of the envelope, Δ, the ice over dust mass ratio, $M_{\rm ice}/M_{\rm dust}$, and the crystalline over amorphous ice mass ratio, $M_{\rm cr}/M_{\rm am}$, for the models shown in Fig. 9. Δ and $M_{\rm ice}/M_{\rm dust}$ increase along the AGB. Ice formation thus indeed becomes more efficient as an AGB star evolves. At the tip of the AGB, $M_{\rm ice}/M_{\rm dust}$ reaches values in the order of $\sim$1 to 2%. In the post-AGB phase, $M_{\rm cr}/M_{\rm am}$ is found to decrease, which is the result of the ongoing amorphization of the ice as the circumstellar envelope moves outwards. This amorphization is complete within 2000 yr. Note that $M_{\rm ice}/M_{\rm dust}$ continues to increase during the post-AGB. This is caused by the fact that in our models we loose dust at the outer radius of the envelope, which decreases the total dust mass, while the grains that are still within the envelope continue to growth ice as they move outwards. This increases the volume fraction of ice on these grains. The net effect is the observed increase of $M_{\rm ice}/M_{\rm dust}$.

5.2.4. The effect of initial mass

Stars with different ZAMS masses, will experience different mass loss rates during the AGB phase, and will evolve through the AGB, post-AGB and PN phases on different time scales. We may expect these differences to influence the ice formation process, suggesting that the process will also be a function of the ZAMS mass. Indeed, model calculations for $<5\ M_{\odot}$ ZAMS mass stars (not shown) suggest that the 3, 43 and 62 μm water ice features become weaker for lower ZAMS masses, and nearly completely disappear for ZAMS masses $\lesssim 3\ M_{\odot}$. Moreover, here we have still ignored the fact that stars with 1.7–4 $M_{\odot}$ ZAMS masses (Gavilán et al. 2005), the exact mass range depending on metallicity (e.g. Groenewegen & Marigo 2004), will actually evolve into carbon stars. Since these stars have stellar atmospheres with an carbon-to-oxygen ratio (C/O) greater than unity, and carbon and oxygen first combine to form CO, there is no freely available oxygen to form water molecules. Hence water ice formation will not occur.

6. Increasing the (crystalline) ice abundance

The predicted 43 and 62 μm crystalline water ice features are very weak, at most a few percent wrt the continuum. This is because almost the entire ice content in the models is amorphous. Contrary to crystalline ice, amorphous ice only has one very broad spectral feature in the 30–100 μm region, making it difficult to distinguish from the continuum. Increasing the crystalline water ice mass will increase the strength of the 43 and 62 μm features, since they are located in the optically thin part of the spectrum. In a companion paper (DP05) we study a large sample of AGB and post-AGB stars, and PNe. The measured abundance of crystalline water ice in these stars is often a few percent of the dust mass, but can be above 10% in extreme cases. While the total amount of ice formed in the models discussed in the previous section is also a few percent, the crystalline ice fraction is consistently about two orders of magnitude lower. This explains the weak predicted 43 and 62 μm crystalline water ice features, and is mainly caused by the efficient amorphization by interstellar UV photons. In this section, we will explore different ways to both increase the total ice abundance, and in particular to reduce the effectiveness of UV amorphization.

6.1. Reheating of ice during the post-AGB phase

One mechanism to increase the crystalline water ice mass is the reheating of amorphous ice during the post-AGB phase. According to the models, the bulk of the ice in the envelopes of AGB stars is amorphous, and expected to form at low temperatures ($T \leq 70$ K). If the amorphous ice that formed in the AGB phase could be reheated during later evolutionary stages, it could anneal into crystalline ice (e.g. Kouchi et al. 1994), strengthening the crystalline ice features.

We studied this possibility for the 5 $M_\odot$ star in Sect. 5. It was found that in the original AGB amorphous ice formation region, the grains were reheated by more than 30 K, and in principle this could have helped to crystallize the amorphous ice. However, the time needed for crystallization is an exponential function of temperature (Kouchi et al. 1994), and in order to crystallize amorphous ice within 1000 years (a time scale applicable to post-AGB evolution) a $\gtrsim$100 K temperature is required (Hoogzaad 2001). We found that the maximum temperature to which the grains were reheated was ~80 K, and this temperature was maintained less than a few thousand years. The crystallization of amorphous ice during the post-AGB/PN phase was therefore found to be unimportant after all.

The presence of crystalline water ice around OH/IR type AGB stars has previously been addressed by Maldoni et al. (2003). Although these authors did not exclude the possibility that ice may indeed condense in a crystalline form, they also considered an alternative scenario. In this scenario, all ice condenses as amorphous ice during the AGB phase, while later a fraction of this ice anneals into crystalline ice. In support of this scenario is the notion that the expected condensation temperature of water ice is near ~100 K, close to the threshold temperature of ~110 K at which the amorphous-to-crystalline phase transition occurs. However, as pointed out by Maldoni et al. (2003), a major objection against this scenario is that, in a given temperature range below 110 K, the crystallization time scales are longer than the transit times of the grains through that temperature range. The amorphous ice in an AGB envelope will therefore have no time to anneal, in agreement with our findings above. Therefore, the formation of crystalline ice through an amorphous-to-crystalline phase transition seems unlikely.

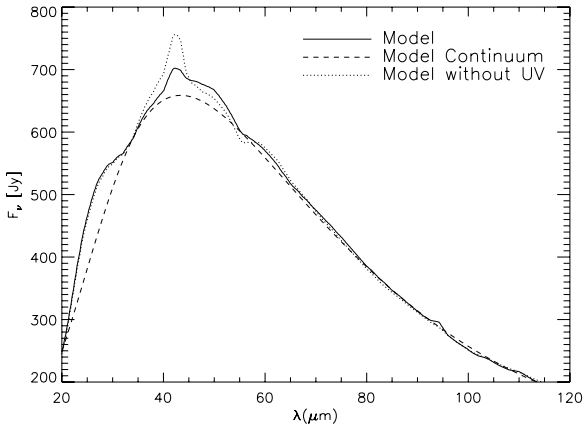

Fig. 10. The effects of an external interstellar UV field on the emergent spectrum of the 5 $M_\odot$ star at $t = 1006$ yr (solid line). Switching off the UV field (dotted line) increases the visibility of the crystalline water ice features near 43 and 62 μm. The dashed line represents the continuum of the original model (i.e. the model with an external interstellar UV field).

6.2. Reducing the interstellar UV radiation field

Another parameter that influences the crystalline water ice mass is the intensity of the interstellar UV radiation field, I_ν. Most importantly, I_ν determines the time scale at which crystalline water ice is amorphisized (Eq. (10)) during the AGB and post-AGB phase. When no UV field is present all crystalline ice produced during the AGB phase may be preserved. Since I_ν may vary within a galaxy, the location of a star within this galaxy will influence the ice formation process.

The effect of an external ISM UV field on the spectrum of the 5 $M_\odot$ star (during the post-AGB phase at $t = 1006$ yr) is shown in Fig. 10. If we switch of the interstellar UV field the 43 and 62 μm crystalline water ice features become much better visible. Still, the effect of amorphous ice remains present in the spectrum. This is due to the fact that during the AGB phase amorphous ice will form naturally on dust grains when the dust temperature is below ~65 K. Without the UV field, the ice composition is approximately 1/3 crystalline, 2/3 amorphous.

6.3. Increasing $\dot{M}/L$

Increasing the mass loss rate at constant luminosity is an effective way to enhance ice formation and to increase the crystalline ice mass. In model 4 (Table 1) we increased the mass loss rate by a factor of 10, producing ~3.2 times more ice per dust grain and 32 times more ice in total. The amount of crystalline ice increased by a factor of 2.3 per dust grain. The total

amount of crystalline ice therefore increased by a factor of 23. The continuum divided spectrum showed a significant increase in the strength of the 43 μm feature (Fig. 4). Also, a lower luminosity promotes ice formation (Paper I). A possible solution to the weak feature problem is therefore to assume that most of the ice formation occurs in periods in which the mass loss rate over luminosity ratio, $\dot{M}/L$, is much larger than on average. In Sect. 7 we investigate this possibility for the post-AGB star HD 161796.

6.4. A clumpy AGB wind

The formation of clumps in the circumstellar envelope during the AGB phase also increases the crystalline water ice mass. Nearby planetary nebulae, such as the Helix nebula, are clearly observed to be clumpy (Redman et al. 2003). In case of the Helix nebula, O'dell & Handron (1996) find that around half of the nebular mass is contained in clumps. The origin of the clumps, and whether they form during the AGB or PN phase, is currently unclear. If the clumps form during the AGB phase, this yields several advantages for (crystalline) water ice formation. First, it will (locally) provide enhanced densities (and possibly lower temperatures) in the envelope, stimulating ice growth. Second, clumps provide additional shielding from interstellar UV radiation, increasing the crystalline over amorphous ice fraction. Both effects may then increase the strength of the 43 and 62 μm crystalline water ice features during post-AGB evolutionary phases.

In order for (strong) crystalline water ice features to remain visible during the subsequent post-AGB and PN phases, the clumps must also provide sufficient shielding from interstellar UV radiation in these stages. However, after a clump has been formed in the AGB phase, it starts to expand. The extinction within the clump will drop, reducing its optical depth. Redman et al. (2003) show that the visual extinction of a clump, $A_{\rm V}$, as a function of time, t, may be given by

$$A_{\rm V} = 10^2 \left(\frac{t}{t_1}\right)^{-1} \qquad (17)$$

where $t_1 = 100$ yr. The initial radius of the clump at time t_1 is assumed to be 10^{14} cm. Whittet et al. (2001) show that the detection threshold for water ice in the Taurus Dark Clouds is $A_{\rm V} = 3.2$. Assuming this number is also valid for clumps in AGB winds we find for the shielding time scale

$$t_{\rm shield} = t_1 \left(\frac{10^2}{A_{\rm V}}\right) \approx 3.1 \times 10^3 \text{ yr}. \qquad (18)$$

The time needed for a 5 $M_\odot$ star to evolve through the post-AGB and PNe phases is 5500 yr (see Blöcker 1995a, and Table 2). A 5 $M_\odot$ star may therefore evolve fast enough for clumps to provide sufficient shielding during the post-AGB and PN phase.

We find that low mass stars clearly evolve too slow for clumps to provide sufficient shielding during the post-AGB and PN phase. For example, stars with ZAMS masses $\leq$3 $M_\odot$ take $\geq$10 000 yr to evolve through the post-AGB and PN phase (Blöcker 1995a). Here it is interesting to note that the low mass star HD 161796 (Sect. 7) only left the AGB phase some 500 years ago, but still shows strong crystalline water ice features. A comparison with $t_{\rm shield}$ shows that clumps may still provide shielding in this source.

6.5. Axisymmetric mass loss on the AGB

Axisymmetric mass loss during the AGB phase may increase the crystalline water ice mass as well. In this scenario, the initially spherical AGB wind gradually enhances near the equator as the star evolves, leading to the formation of a dusty equatorial torus. The equatorial wind will provide enhanced densities, possibly lower temperatures, and increased shielding from interstellar UV radiation. All these effects increase the relative fraction of crystalline over amorphous ice. Indeed, near infrared (2.4–3.8 μm) spatially resolved spectroscopy of the post-AGB star M 1-92 (Eiroa & Hodapp 1989) suggest that water ice is located in its dusty torus, where the outer portions of the torus are found to be free of ice. The 3 μm ice feature indicates that the ice in the torus is primarily crystalline.

The formation of an axisymmetric wind during the AGB phase may reconcile the mass loss rates predicted by Blöcker (1995b, see Eq. (13)), and the large $\dot{M}/L$ ratio needed to explain the strength of crystalline water ice features in post-AGB stars (Sect. 6.3). Compared to a spherically symmetric wind, an axisymmetric wind naturally mimics a larger $\dot{M}/L$ ratio in the equatorial regions, without the need for a higher overall mass loss rate $\dot{M}$. The *artificial* increase of $\dot{M}/L$ near the equator stimulates the ice formation process, while keeping $\dot{M}$ well within the predicted range.

6.6. Water vapour abundances

Finally, following Paper I, we assumed that the initial water vapour abundance (by number with respect to H) is $\varepsilon_0^{\rm H2O} = 1 \times 10^{-4}$. This value is applicable to the circumstellar envelopes of oxygen-rich evolved stars (González-Alfonso & Cernicharo 1999). Still, the water vapour abundance is set by the C/O in the stellar atmosphere, which changes with stellar evolution (Lattanzio & Wood 2004; Herwig 2005). The water vapour abundance may therefore change as the star evolves, also affecting the total amount of (crystalline) water ice that will form.

7. Application to HD 161796

As a test case for modeling ice features around AGB and post-AGB stars, we now turn to the well-known post-AGB star HD 161796 which shows prominent 43 and 62 μm crystalline water ice features (see e.g. Molster et al. 2002; Hoogzaad et al. 2002, and DP05). In this source the strength of the 43 μm feature is on the order of 60% wrt the continuum, while the 62 μm feature is 15% wrt the continuum. HD 161796 is a high galactic latitude population II post-AGB star (Fernie & Garrison 1984), which suggests a low progenitor mass. Consequently, we might expect even weaker features than predicted for the 3 $M_\odot$ star mentioned in Sect. 5.2.4. Clearly, this is not so. As we will discuss next, the reason for this large discrepancy is related to the assumed $\dot{M}/L$ ratio for the stars in our model calculations.

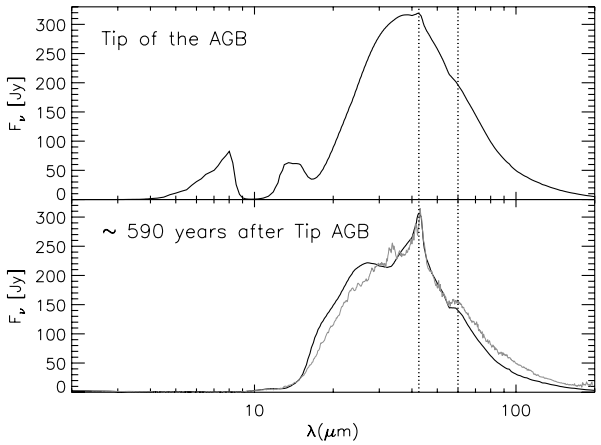

Fig. 11. Model spectra for the post-AGB star HD 161796. The upper panel shows a model spectrum for the star as it would have appeared on the tip of the AGB, some 600 year ago. The lower panel shows a model spectrum for the post-AGB phase, based on (circum-)stellar parameters for HD 161796 taken from Hoogzaad et al. (2002), together with the observed ISO spectrum (grey line). The relatively strong crystalline water ice features of HD 161796 in both the AGB and post-AGB phase, are explained by the large $\dot{M}/L$ ratio for this star. For a detailed discussion see Sects. 6.3 and 7.

In Fig. 11 we show the observed ISO spectrum of HD 161796 (lower panel, taken from DP05), together with two model calculations for this star. In the upper panel we show a predicted spectrum for the star as it would have appeared on the tip of the AGB, some 600 year ago, while in the lower panel we model the spectrum as it appears now in the post-AGB phase. The parameters for the post-AGB model were taken from Hoogzaad et al. (2002). For the tip of the AGB model, we assumed that the luminosity of the star was the same as in the post-AGB phase ($L \approx 3.1 \times 10^3\ L_\odot$). Furthermore, we assumed that the mantle of the star was extended and fully convective such that it would have been on a Hayashi-track while on the AGB (see Schönberner 1979). Its effective temperature would have been given by $T_{\rm eff} = 10^{3.8}\ (L/L_\odot)^{-0.08} \approx 3300$ K. This approximation likely yields a too high effective temperature. However, for a sufficiently optically thick envelope the exact value of $T_{\rm eff}$ is irrelevant for the emerging spectrum (Sect. 5.1). The outer radius of the envelope was assumed to be the same as for the post-AGB model. The mass loss rate on the tip of the AGB was taken to be $\dot{M} = 5.1 \times 10^{-4}\ M_\odot$/yr (Hoogzaad et al. 2002).

The post-AGB model for HD 161796 (lower panel Fig. 11) still shows some clear discrepancies with the ISO spectrum. These include an overestimation of the flux near 20 μm, and an underestimation of the flux near 60 μm. These discrepancies may be resolved if the envelope is made somewhat colder, i.e. by moving the inner radius outwards. Important for the current discussion is that the predicted strength of the water ice features is now in much better agreement with the observation. In particular the 43 μm feature is well fitted by the model. The water ice features are also much more pronounced in the AGB phase, and the ice formation process during this phase is more efficient. For the depletion we now find $\Delta \approx 50\%$, while for the ice mass fraction we find $M_{\rm ice}/M_{\rm dust} = 12\%$, assuming a dust to gas ratio of 3.7×10^{-3} (Hoogzaad et al. 2002). Also, much more crystalline ice forms compared to the previous models (~12% of the total ice mass).

The more efficient ice formation process and stronger water ice features for HD 161796 are caused by its relatively large $\dot{M}/L$ ratio compared to those from the evolutionary tracks of Blöcker (1995b) and Blöcker (1995a). On the tip of the AGB, this ratio is respectively a factor 68 and 18 larger than those for the 3 and 5 $M_\odot$ stars listed in Table 2. For a model less massive than 3 $M_\odot$, which may be more applicable for HD 161796, the difference will likely be even larger. The above considerations thus suggest that the mass loss rate formula given by Blöcker (1995b) in Eq. (13) still greatly under-predicts the actual mass loss rate on the AGB. Finally note that a larger $\dot{M}/L$ ratio will also increase the column densities discussed in Sect. 5.2.2, which may bring them closer to the observed values.

8. Summary and conclusions

In this paper we presented a detailed model that predicts the infrared spectra of AGB stars and Red Supergiants under the influence of ice formation. The model self-consistently takes into account the formation of water ice by gas phase condensation on pre-existing silicate grains.

We find that in a typical AGB model ($L = 10^4\ L_\odot$, $\dot{M} = 10^{-4}\ M_\odot$/yr, $v_{\rm exp} = 15$ km s^{-1}) the ice mass fraction is 2%. Only 1% of the ice, i.e. 0.02% of the total dust mass, is expected to be crystalline. This leads to no detectable spectral structure in the 30–100 μm region since the resulting features are broad and very weak.

In a parameter study we have explored effects that may increase the crystalline ice fraction. A larger wind density due to a higher mass loss rate or a decreased gas outflow velocity both enhance ice formation and reduce the destructive effects of sputtering. Sputtering is also reduced by lowering the stellar luminosity. Since ice formation is most efficient on small grains, changing the dust size distribution to favor small grains also increases the amount of ice that is formed, and consequently the strength of the features. However, even in extreme cases, the features reach a strength of at most 3% above continuum on the AGB.

In order to study the visibility of ice features in the post-AGB and PN phase, we followed the evolution of the spectrum due to the expansion of the dust shell and the change in stellar temperature, using post-AGB tracks for a 5 $M_\odot$ star. For this 5 $M_\odot$ star, a weak 43 μm is visible throughout the post-AGB phase. In the 3 μm region an absorption feature is seen which is first dominated by crystalline ice and later by amorphous ice. This change in lattice structure is caused by the interstellar UV radiation field. With progressing shell expansion this field penetrates deeper into the shell and amorphisizes the initially crystalline ice. The same amorphization makes the 43 μm feature disappear when the star enters the planetary nebula phase. We find that the strength of the 3, 43 and 62 μm features decreases with decreasing ZAMS mass.

The overall weakness of the ice features is not caused by the amount of ice formed, but by the fact that it is amorphous. Our model calculations show that a significant fraction of the

ice (typically 30%) initially forms as crystals, but is quickly amorphisized by interstellar UV radiation. In order to increase the amount of crystalline ice, the dust grains must be protected from UV radiation. We have considered a number of ways to do this, including clumpiness of the wind, axisymmetric mass loss, and very high mass loss rate over luminosity ($\dot{M}/L$) ratios. All these mechanisms increase the column densities and therefore the optical depth at UV wavelengths. We showed that all three mechanisms can provide protection, and have demonstrated this for the high $\dot{M}/L$ scenario with a model fit to the post-AGB star HD 161796. We were able to reproduce the strong crystalline ice features seen in this star by combining a low luminosity with a very high mass loss rate. The $\dot{M}/L$ ratio required to fit HD 161796 exceeds the one derived from the mass loss rate formulae used in stellar evolution calculations by Blöcker (1995b). Therefore, HD 161796 must have undergone a very strong superwind phase (either spherically or only in an equatorial region) just prior to leaving the AGB. This strong superwind is not only required to fit the overall SED, but also too provide the conditions necessary to form large amounts of ice and to keep this ice crystalline.

The presence and strength of crystalline ice features in AGB and post-AGB stars therefore provides an independent diagnostics for the conditions present during the superwind phase at the tip of the AGB. Further studies into the ice formation, in particular detailed fits to individual objects taking into account both the 3 μm and the 30–100 μm spectral regions will likely provide a better insight into the evolution of such objects.

Acknowledgements. We thank M. Min for help with implementing the calculation of optical properties, and L.B.F.M. Waters and an anonymous referee for helpful comments on the original manuscript.

References

Bertie, J. E., Labbé, H. J., & Whalley, E. J. 1969, J. Chem. Phys., 50, 4501
Black, J. H. 1994, in The First Symposium on the Infrared Cirrus and Diffuse Interstellar Clouds, ASP Conf. Ser., 58, 355
Blöcker, T. 1995a, A&A, 299, 755
Blöcker, T. 1995b, A&A, 297, 727
Bohren, C. F., & Huffman, D. R. 1983, Absorption and Scattering of Light by Small Particles (New York: Wiley)
Bouwman, J. 2001, Ph.D. Thesis University of Amsterdam
Charnley, S. B., & Smith, R. G. 1993, in Planetary Nebulae, IAU Symp., 155, 329
Clayton, D. D., & Nittler, L. R. 2004, ARA&A, 42, 39
Daulton, T. L., Bernatowicz, T. J., Lewis, R. S., et al. 2003, Geochim. Cosmochim. Acta, 67, 4743
Dijkstra, C., Dominik, C., Hoogzaad, S. N., de Koter, A., & Min, M. 2003a, A&A, 401, 599
Dijkstra, C., Waters, L. B. F. M., Kemper, F., et al. 2003b, A&A, 399, 1037
Dorschner, J., Begemann, B., Henning, T., Jaeger, C., & Mutschke, H. 1995, A&A, 300, 503
Eiroa, C., & Hodapp, K.-W. 1989, A&A, 223, 271
Fernie, J. D., & Garrison, R. F. 1984, ApJ, 285, 698
Fluks, M. A. 1998, Ph.D. Thesis University of Amsterdam
Gavilán, M., Buell, J. F., & Mollá, M. 2005, A&A, 432, 861
González-Alfonso, E., & Cernicharo, J. 1999, ApJ, 525, 845
Groenewegen, M., & Marigo, P. 2004, in Asymptotic Giant Branch Stars, ed. H. J. Habing, & H. Olofsson, Astronomy and Astrophysics Library (Springer), Chapter 3
Habing, H. J. 1996, A&AR, 7, 97
Habing, H. J., & Olofsson, H. 2004, Asymptotic Giant Branch Stars, Astronomy and Astrophysics Library (Springer)
Herwig, F. 2005, ARA&A, 43, 435
Hoogzaad, S. N. 2001, Master Thesis Vrije Universiteit (VU) Amsterdam
Hoogzaad, S. N., Molster, F. J., Dominik, C., et al. 2002, A&A, 389, 547
Hudgins, D. M., Sandford, S. A., Allamandola, L. J., & Tielens, A. G. G. M. 1993, ApJS, 86, 713
Hurley, J. R., Pols, O. R., & Tout, C. A. 2000, MNRAS, 315, 543
Izzard, R. G., Tout, C. A., Karakas, A. I., & Pols, O. R. 2004, MNRAS, 350, 407
Jura, M., & Morris, M. 1985, ApJ, 292, 487
Kemper, F., Waters, L. B. F. M., de Koter, A., & Tielens, A. G. G. M. 2001, A&A, 369, 132
Kessler, M. F., Steinz, J. A., Anderegg, M. E., et al. 1996, A&A, 315, L27
Kim, S.-H., Martin, P. G., & Hendry, P. D. 1994, ApJ, 422, 164
Kouchi, A., & Kuroda, T. 1990, Nature, 344, 134
Kouchi, A., Yamamoto, T., Kozasa, T., Kuroda, T., & Greenberg, J. M. 1994, A&A, 290, 1009
Lattanzio, J., & Wood, P. 2004, in Asymptotic Giant Branch Stars, ed. H. J. Habing, & H. Olofsson, Astronomy and Astrophysics Library (Springer), Chapter 2
Lepault, J., Freeman, R., & Dubochet, J. 1983, J. Microscopy, 132, 3
Maldoni, M. M., Egan, M. P., Smith, R. G., Robinson, G., & Wright, C. M. 2003, MNRAS, 345, 912
Mathis, J. S., Mezger, P. G., & Panagia, N. 1983, A&A, 128, 212
Mathis, J. S., Rumpl, W., & Nordsieck, K. H. 1977, ApJ, 217, 425
Meixner, M., Ueta, T., Bobrowsky, M., & Speck, A. 2002, ApJ, 571, 936
Meyer, A. W., Smith, R. G., Charnley, S. B., & Pendleton, Y. J. 1998, AJ, 115, 2509
Molster, F. J., Lim, T. L., Sylvester, R. J., et al. 2001, A&A, 372, 165
Molster, F. J., Waters, L. B. F. M., Tielens, A. G. G. M., & Barlow, M. J. 2002, A&A, 382, 184
Moore, M. H., & Hudson, R. L. 1992, ApJ, 401, 353
Nittler, L. R., Alexander, C. M. O., Gao, X., Walker, R. M., & Zinner, E. 1997, ApJ, 483, 475
O'dell, C. R., & Handron, K. D. 1996, AJ, 111, 1630
Omont, A., Forveille, T., Moseley, S. H., et al. 1990, ApJ, 355, L27
Redman, M. P., Viti, S., Cau, P., & Williams, D. A. 2003, MNRAS, 345, 1291
Sahai, R., Zijlstra, A., Sánchez Contreras, C., & Morris, M. 2003, ApJ, 586, L81
Schönberner, D. 1979, A&A, 79, 108
Suh, K. 1999, MNRAS, 304, 389
Sylvester, R. J., Kemper, F., Barlow, M. J., et al. 1999a, A&A, 352, 587
Sylvester, R. J., Kemper, F., Barlow, M. J., et al. 1999b, A&A, 352, 587
Vassiliadis, E., & Wood, P. R. 1994a, VizieR Online Data Catalog, 209, 20125
Vassiliadis, E., & Wood, P. R. 1994b, ApJS, 92, 125
Warren, S. G. 1984, Appl. Opt., 23, 1206
Weinberger, R., Dengel, J., Hartl, H., & Sabbadin, F. 1983, ApJ, 265, 249
Whittet, D. C. B., Gerakines, P. A., Hough, J. H., & Shenoy, S. S. 2001, ApJ, 547, 872